

BOSTON UNIVERSITY  
GRADUATE SCHOOL OF ARTS AND SCIENCES

Dissertation

**MEASUREMENT OF THE ANOMALOUS MAGNETIC  
MOMENT OF THE POSITIVE MUON TO .SOMETHING  
PARTS PER BILLION**

by

**NICHOLAS BRENNAN KINNAIRD**

B.S., University of Texas at Austin, 2013  
B.S., University of Texas at Austin, 2013  
M.A., Boston University, 2016

Submitted in partial fulfillment of the  
requirements for the degree of  
Doctor of Philosophy

2019

© 2019 by  
NICHOLAS BRENNAN KINNAIRD  
All rights reserved

Approved by

First Reader

---

B. L. Roberts, PhD  
Professor of Physics

Second Reader

---

R. M. Carey, PhD  
Professor of Physics

Third Reader

---

J. P. Miller, PhD  
Professor of Physics

## **Dedication**

I dedicate this thesis to

## Acknowledgments

Here go all your acknowledgments. You know, your advisor, funding agency, lab mates, etc., and of course your family.

As for me, I would like to thank Jonathan Polimeni for cleaning up old LaTeX style files and templates so that Engineering students would not have to suffer typesetting dissertations in MS Word. Also, I would like to thank IDS/ISS group (ECE) and CV/CNS lab graduates for their contributions and tweaks to this scheme over the years (after many frustrations when preparing their final document for BU library). In particular, I would like to thank Limor Martin who has helped with the transition to PDF-only dissertation format (no more printing hardcopies – hooray !!!)

The stylistic and aesthetic conventions implemented in this LaTeX thesis/dissertation format would not have been possible without the help from Brendan McDermot of Mugar library and Martha Wellman of CAS.

Finally, credit is due to Stephen Gildea for the MIT style file off which this current version is based, and Paolo Gaudiano for porting the MIT style to one compatible with BU requirements.

Janusz Konrad  
Professor  
ECE Department

**MEASUREMENT OF THE ANOMALOUS MAGNETIC  
MOMENT OF THE POSITIVE MUON TO .SOMETHING  
PARTS PER BILLION**

(Order No. )

**NICHOLAS BRENNAN KINNAIRD**

Boston University, Graduate School of Arts and Sciences, 2019

Major Professor: B. L. Roberts, Professor of Physics

**ABSTRACT**

Have you ever wondered why this is called an *abstract*? Weird thing is that its legal to cite the abstract of a dissertation alone, apart from the rest of the manuscript.

# Contents

<b>1</b>	<b>Introduction</b>	<b>1</b>
1.1	Magnetic Dipole Moments . . . . .	2
1.2	Background . . . . .	3
1.2.1	Definitions . . . . .	3
1.2.2	Experiment History . . . . .	3
1.3	Theory . . . . .	3
1.3.1	QED . . . . .	3
1.3.2	Electroweak . . . . .	3
1.3.3	HVP . . . . .	3
1.3.4	HLbL . . . . .	6
1.3.5	BSM . . . . .	6
<b>2</b>	<b>Muon g-2 at Fermilab, E989</b>	<b>7</b>
2.1	Principle Technique . . . . .	7
2.2	Accelerator . . . . .	10
2.3	Injection . . . . .	10
2.4	Storage . . . . .	11
2.5	Detector Systems . . . . .	11
2.5.1	T0 . . . . .	11
2.5.2	IBMS . . . . .	13
2.5.3	Fiber Harps . . . . .	15
2.5.4	Calorimeters . . . . .	15

2.5.5	Laser Calibration System . . . . .	18
2.5.6	Straw Trackers . . . . .	19
<b>3</b>	<b>Magnetic Field Measurement</b>	<b>23</b>
3.1	Trolley . . . . .	23
3.2	Opera Simulations . . . . .	23
<b>4</b>	<b>Straw Tracking Analysis</b>	<b>24</b>
4.1	Straw Tracking Intro . . . . .	24
4.2	Track Finding . . . . .	24
4.3	Track Fitting . . . . .	24
4.3.1	Track Fitting Formalism . . . . .	27
4.4	Track Extrapolation . . . . .	34
<b>5</b>	<b><math>\omega_a</math> Measurement</b>	<b>37</b>
5.1	Data . . . . .	37
5.2	Spectra Making . . . . .	37
5.2.1	Clustering . . . . .	37
5.2.2	Histogramming . . . . .	37
5.3	Fitting . . . . .	37
5.4	Systematic Errors . . . . .	37
<b>6</b>	<b>Conclusion</b>	<b>38</b>
6.1	Final Value . . . . .	38
<b>A</b>	<b><math>g</math> for Spin-1/2 Particles and Beyond</b>	<b>39</b>
<b>B</b>	<b>Ratio Method Derivation</b>	<b>42</b>
B.1	Ratio Function . . . . .	42
B.2	Ratio Function Errors . . . . .	47
<b>Curriculum Vitae</b>		<b>50</b>

## List of Tables

# List of Figures

1.1	AlexKPaperComparison	4
1.2	testfeynmanpicture2	4
1.3	testfeynmanpicture2	5
1.4	testfeynmanpicture2	5
1.5	testfeynmanpicture2	6
2.1	Decay Diagrams	8
2.2	Muon Decay - Max Energy Positron	9
2.3	ring	10
2.4	T0 Counter	12
2.5	T0 Pulses	13
2.6	IBMS Models	14
2.7	IBMS Positions	14
2.8	Fiber Harp	16
2.9	Fiber Harp Measurement	17
2.10	TrackerCaloWithLines	19
2.11	Tracker module	21
2.12	Tracker module arrangement	22
4.1	TrackAndCaloHit	25
4.2	pileupEvent	26
4.3	Vertical magnetic field from Opera2D	27
4.4	Horizontal magnetic field from Opera2D	28

4.5	Birds Eye View of Extrapolation	35
4.6	Beam spot extrapolation	36

## List of Abbreviations

ppm	.....	parts per million
ppb	.....	parts per billion
BNL	.....	Brookhaven National Laboratory
FNAL	.....	Fermi National Accelerator Laboratory
SM	.....	Standard Model
SiPM	.....	Silicon Photo-Multiplier
Geane	.....	Geometry and Error Propagation
Geant4	.....	Geometry and Tracking 4
WFD	.....	waveform digitizer
PMT	.....	photo-multiplier tube
IBMS	.....	inflector beam monitoring system
CBO	.....	coherent betatron oscillation

# Chapter 1

## Introduction

The prevailing theory for particle physics, the Standard Model (SM), has had tremendous success in describing our universe. It has been used to predict and explain a wide variety of phenomena and particles, their properties and interactions, to great precision. However, in spite of its success in explaining nearly all experimental results, there exist unanswered questions about our universe. Some of these include the matter-antimatter asymmetry, the source of mass for the neutrinos, the existence of dark matter, and an inability to fully incorporate our best theory of gravitation. Many particle physics experiments are being devised and conducted around the world in order to shed light on these questions and improve our understanding of reality. One such particular experiment is the Fermilab Muon  $g - 2$  Experiment (E989) underway at the Fermi National Accelerator Laboratory (FNAL) located in Batavia, Illinois.

I have been a part of the E989 experiment since I began my graduate degree six years ago. Three years ago I moved from Boston to Batavia to be where the action is. This dissertation will describe in detail the work which I have done for the experiment. Chapter 1 will provide experimental and theoretical background to the experiment, as well its motivation. Chapter 2 will describe the experiment in broad strokes. Chapter 3 will describe the magnetic field portion of the experiment, and magnetic field simulations I conducted. Chapter 4 will describe the straw tracking detectors and their measurements, including the track fitting I wrote. Chapter 5

will describe The frequency measurement portion of the experiment, and detail the analysis results from data taken in the first half of 2018. Finally, Chapter 6 will conclude the thesis and the important results contained within.

## 1.1 Magnetic Dipole Moments

In order to understand the purpose of the Fermilab Muon  $g - 2$  Experiment, first we need to understand what the  $g$  in  $g - 2$  is, and why we might want to measure it. All particles have intrinsic properties which describe those particles. One of those properties is the so called magnetic dipole moment. This property of a particle is related to its spin through the equation

$$\vec{\mu} = g \frac{Qe}{2m} \vec{s}, \quad (1.1)$$

where  $\vec{\mu}$  is the magnetic dipole moment of a particle,  $\vec{s}$  is its spin vector,  $m$  is its mass,  $e$  is the positive charge of an electron,  $Q = \pm 1$ , and  $g$  is the gyromagnetic ratio, or "g-factor". Here and following  $c$  and  $\hbar$  have been set to 1. In a Dirac theory,  $g$  is equal to 2 for spin-1/2 particles [**cite dirac or something**]. See Appendix A for a derivation of this result.

It has the goal of measuring the magnetic moment of the muon, proportional to the  $g$  in  $g - 2$ , to high precision in order to compare to SM theoretical predictions. Because the magnetic moment of particles couple to all existing particles, known or unknown, (source this? reference to a later section?) this provides an avenue through which theories might be constrained, and new physics narrowed down. Indeed this experiment is the latest in a line of such experiments which have measured the magnetic moment of the muon over the past several decades, the last of which measured the magnetic moment of the muon to .54 parts per million (ppm) at Brookhaven National Laboratory (BNL) in 2001 [1].

## 1.2 Background

The previous  $g-2$  experiment at BNL measured a discrepancy in the magnetic moment of the muon between theory and experiment with a 2.2 - 2.7 standard deviation. (Cite the final report again?) That disagreement has since grown above  $3\sigma$  [2], depending on the theoretical analysis approaches used.

### 1.2.1 Definitions

$$a = \frac{g - 2}{2} \quad (1.2)$$

-would it be worthwhile to include my derivation on the magnetic moment like in my hep presentation? - in the appendix

### 1.2.2 Experiment History

-do I want this? I'm sort of already talking about this for E821 in the intro and background - I don't think I want to go into the older experiments

## 1.3 Theory

- see papers cited in my HEP2 class paper - and then look for new ones - Fred Jegerlehner's book - perhaps Matthew Schwartz's short paper

Feynmann diagrams made with [3, 4].

### 1.3.1 QED

### 1.3.2 Electroweak

### 1.3.3 HVP

-clean up hadronic section formatting - figure out exactly how I want to lay out the theory part in relation to the introduction

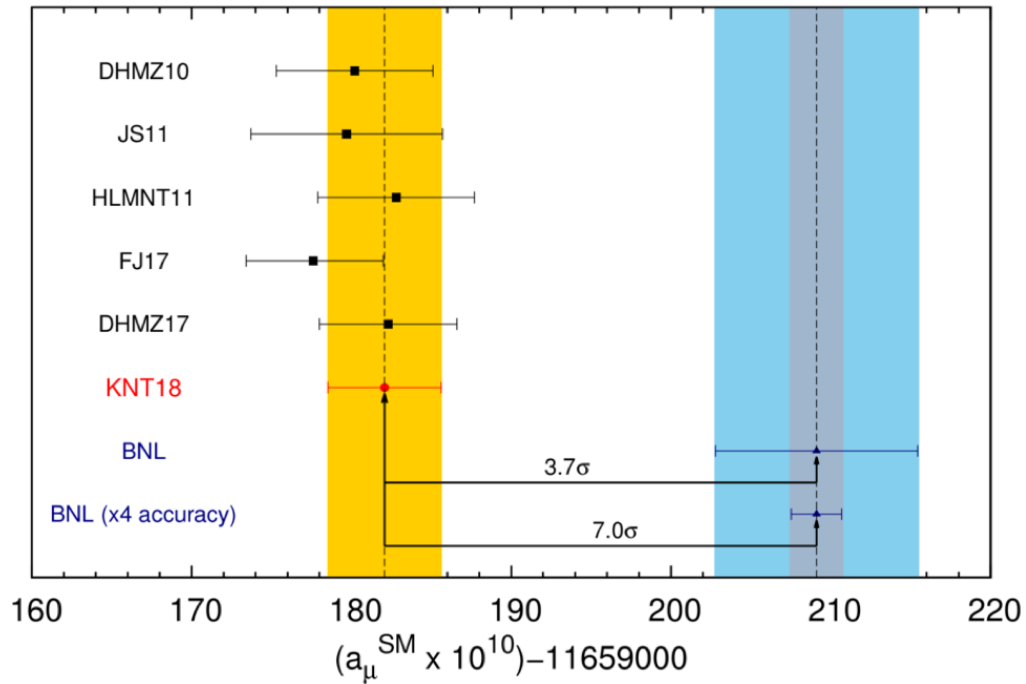


Figure 1.1: any figures that are directly lifted from someone else's work needs to be cited everytime they're used I believe, even if I cite that work in the text somewhere - [2]

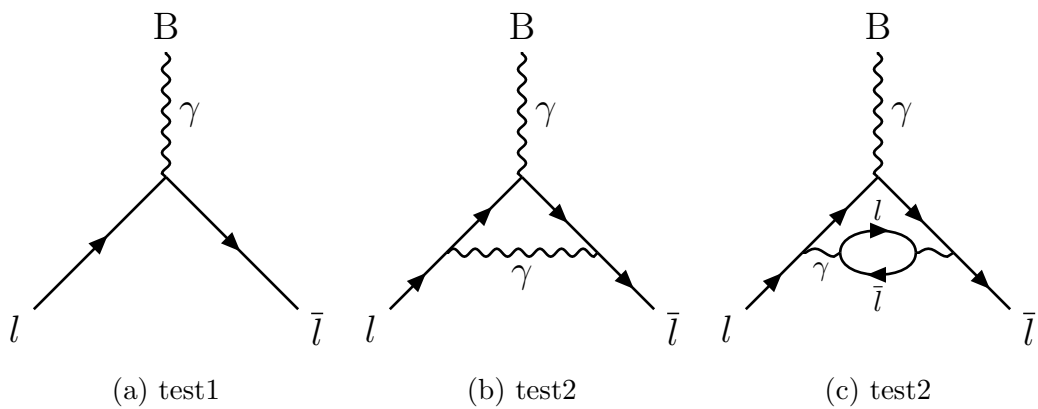


Figure 1.2: clean up and possibly replace

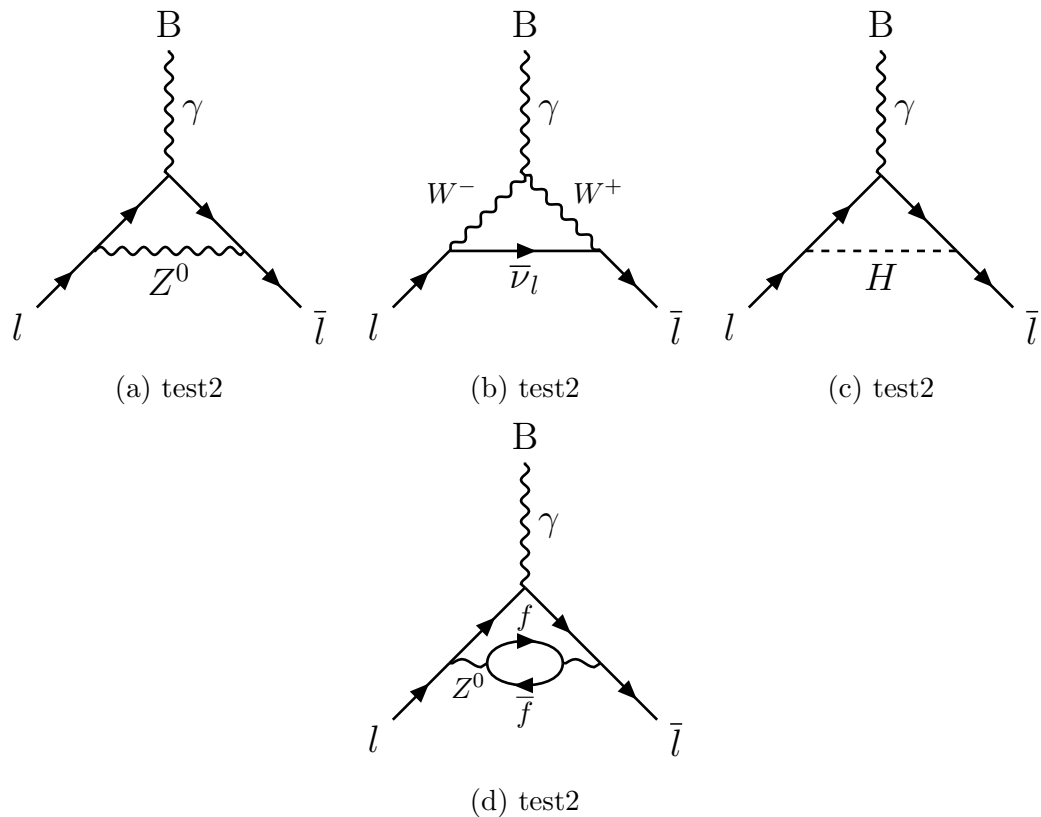


Figure 1.3: clean up and possibly replace

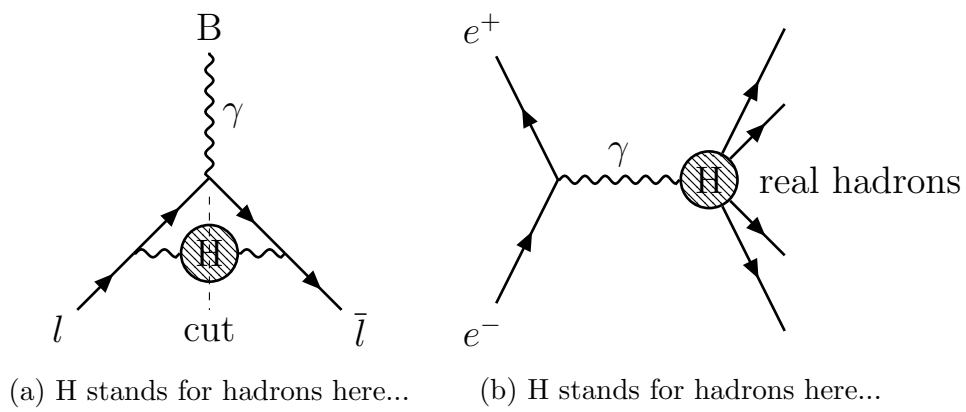


Figure 1.4: clean up and possibly replace

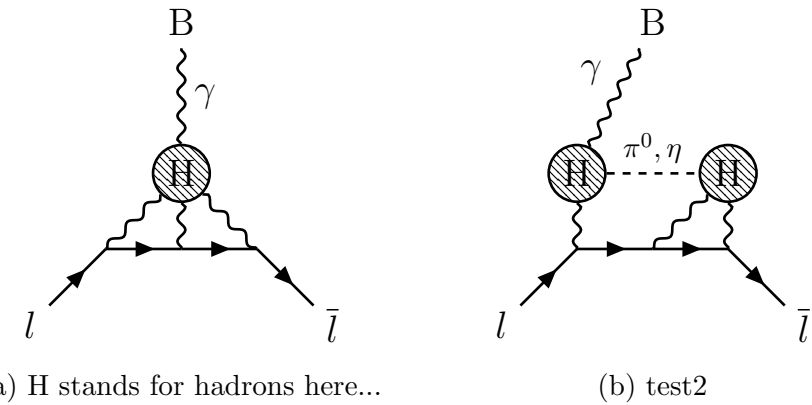


Figure 1.5: clean up and possibly replace

### 1.3.4 HLbL

### 1.3.5 BSM

## Chapter 2

# Muon g-2 at Fermilab, E989

### 2.1 Principle Technique

In a dipole magnetic field, particles will orbit at the cyclotron frequency

$$\omega_c = -\frac{Qe}{\gamma m}B, \quad (2.1)$$

and their spins will turn at the precession frequency

$$\omega_s = -g\frac{Qe}{2m}B - (1 - \gamma)\frac{Qe}{\gamma m}B, \quad (2.2)$$

where  $Q = \pm 1$  and  $e > 0$ . The difference between these two frequencies gives

$$\omega_a = \omega_s - \omega_c = -\frac{g - 2}{2}\frac{Qe}{m}B = -a\frac{Qe}{m}B, \quad (2.3)$$

a measurable frequency that is directly proportional to the property of significance, the anomaly  $a$ . By measuring the spin difference frequency for muons and the magnetic field  $B$ ,  $a_\mu$  can be determined. In the presence of an electric field, which is useful in storing the muon beam within a dipole magnetic field, this expands to

$$\vec{\omega}_a = -\frac{Qe}{m}[a_\mu \vec{B} - (a_\mu - \frac{1}{\gamma^2 - 1})(\vec{\beta} \times \vec{E})], \quad (2.4)$$

where now the measurable quantities are vector quantities. Finally, for realistic cases of muon momentum which is non-orthogonal to the magnetic field, the spin difference

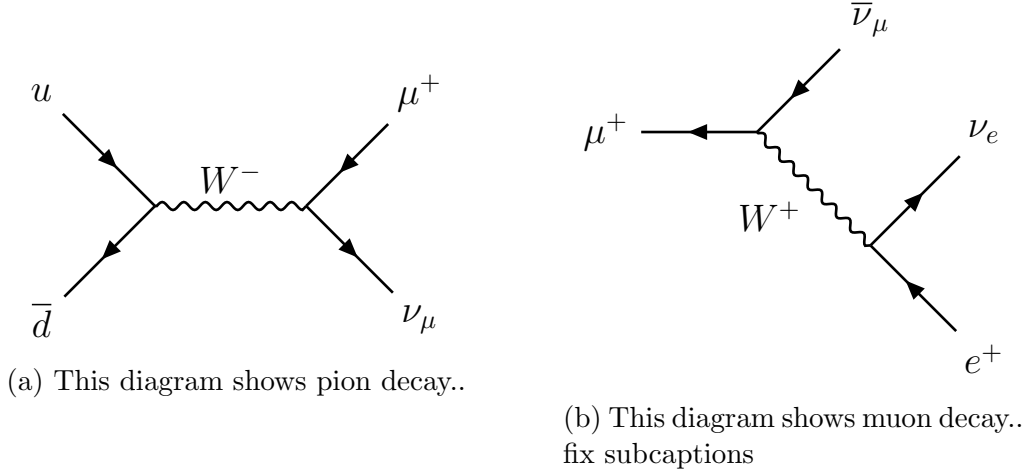


Figure 2.1: These diagrams show pion and muon decay...

frequency becomes

$$\vec{\omega}_a = -\frac{Qe}{m} [a_\mu \vec{B} - a_\mu \left(\frac{\gamma}{\gamma + 1}\right) (\vec{\beta} \cdot \vec{B}) \vec{B} - \left(a_\mu - \frac{1}{\gamma^2 - 1}\right) (\vec{\beta} \times \vec{E})]. \quad (2.5)$$

If the motion of the muons is largely perpendicular to the magnetic field, then the second term is small and can be corrected for. If the particles have a momentum of approximately 3.09 GeV/c, the so called “magic momentum,” then the third term is small and can be corrected for. These will be talked about later.

In order to measure the spin difference frequency of the muon, a clever technique is used. Decay muons in the pion rest frame are 100% polarized due to conservation of angular momentum and the fact that the decay neutrino must have a specific helicity. Within a pion beam then the highest and lowest energy decay muons are polarized. Muons will decay to positrons with a lifetime of about 2.2  $\mu$ s, and the positrons with the highest energies will be correlated with the muon spin, a so called “self-analyzing” decay. The single available decay state for a maximum energy positron illustrates this in Figure ???. Thus, by aquiring a large sample of polarized muons and injecting them into a storage ring

## Muon decay in the rest frame

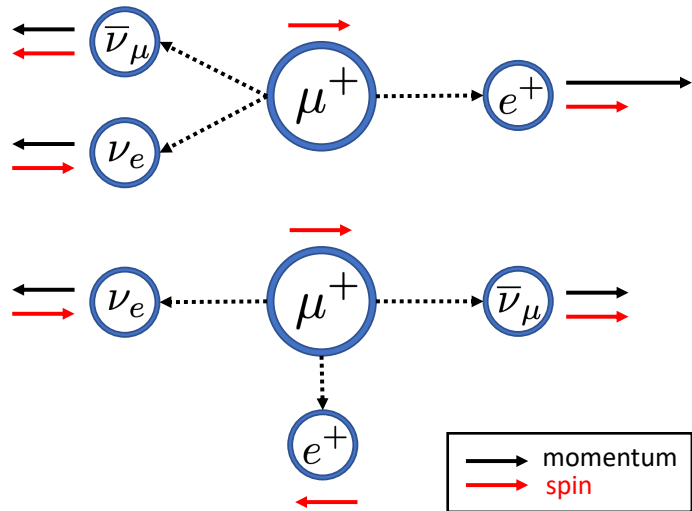


Figure 2.2: improve this caption! The single available decay state for maximum energy decay positrons. Due to the conservation of angular momentum and the single possible helicity states of the decay neutrino and anti-neutrino, the spin of the decay positron is exactly equal to the spin of the muon at the time of the decay.

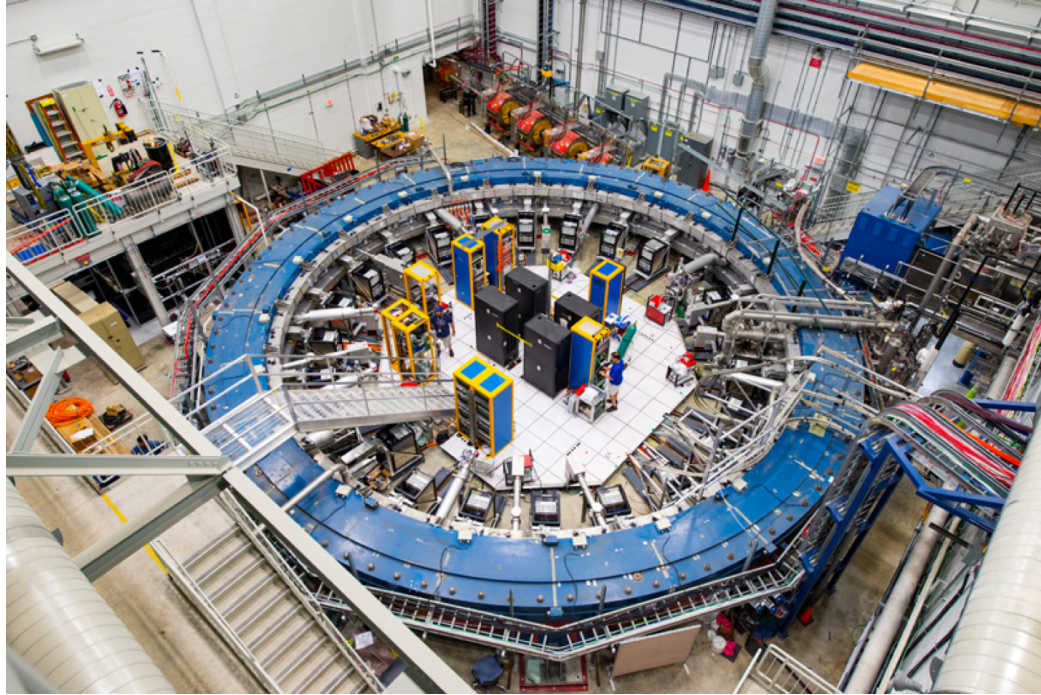


Figure 2·3: clean up and possibly replace

-explain the physics -explain how we get at the physics with our ring and detectors  
 -parity violation -actually write out the decay states before explaining some things -  
 well shouldn't these have been talked about before?? maybe not -decay probabilities  
 and all that -don't measure all decay positrons -By injecting a large ensemble of  
 muons and -by measuring a subset of ensemble of muons.... -Careful with spin vs  
 polarization

## 2.2 Accelerator

[5]

## 2.3 Injection

the inflector

## 2.4 Storage

kickers and quads

## 2.5 Detector Systems

-how should I order these sections? perhaps by what the beam sees in order?

### 2.5.1 T0

In order to align the decay positron spectra in time from fill to fill, an entrance “T0” detector is used. It is made up of a scintillating paddle connected to two (2-inch Hammatsu?) PMTs (photo-multiplier tubes), and is placed just on the outside of the ring before the inflector. See Figure 2·4. One of the PMTs serves as the actual T0 counter which provides an average time of the incoming beam with which to align the fills. The second paddle acts as a magnitude counter to serve as a proxy for the fill intensity. Together they provide a measure of the injected beam profile in time. The varying intensity and bunch shapes can be seen as shown in Figure 2·5.

-might use the same WFD as Calo 1... -cite all this, with the TDR or hopefully something else [6] - can possibly just cite DocDBs as well - need to figure that out -double check all this - just wrote from memory, also add detail - might want to just explain things better too, “one PMT with low pe stats and one with high pe stats” and how that works in the way I’ve already described above - ND (neutral density filters) one at 1% one at 10% -if I use p.e. include it in the abbreviations -get a picture of a T0 output from the midas page, also possibly comparing various bunches -docDB 10911 for details -docDB 10162 for pictures by Hannah

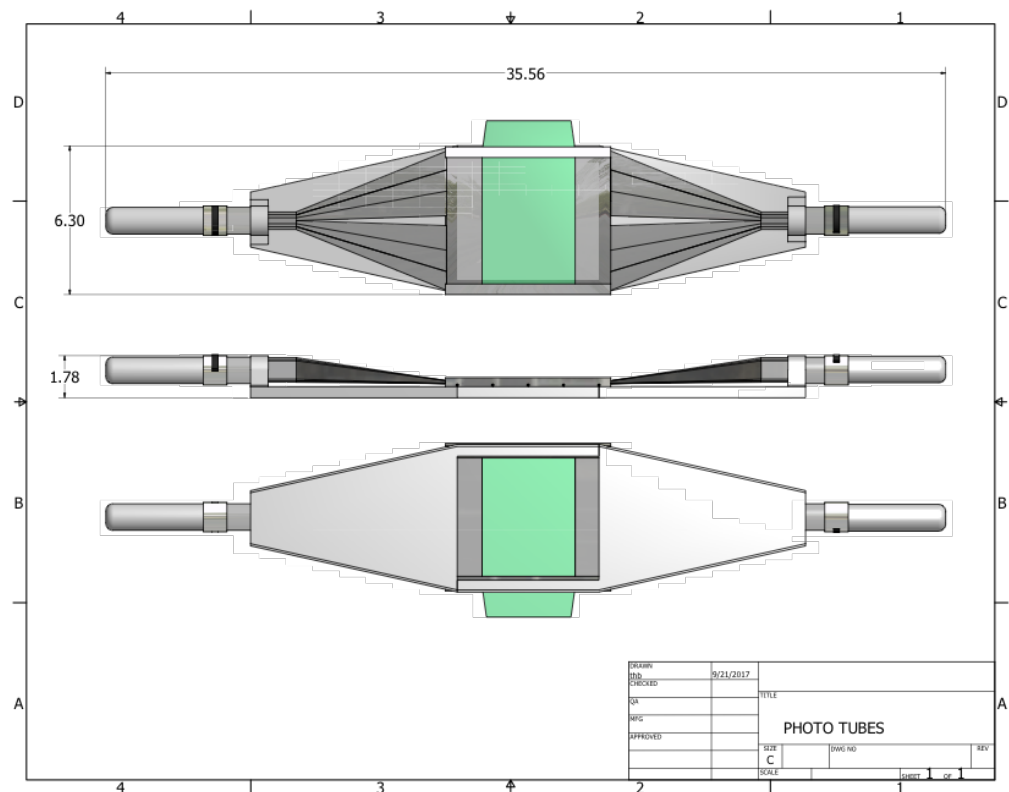


Figure 2.4: Shown is the T0 entrance counter. In the center in green is the scintillator, which connects with light guides to PMTs on the left and right. Each PMT has a separate ND (what's this?) filter to modify the light output into each PMT to configure one more for fill timing, and the other for fill intensity.

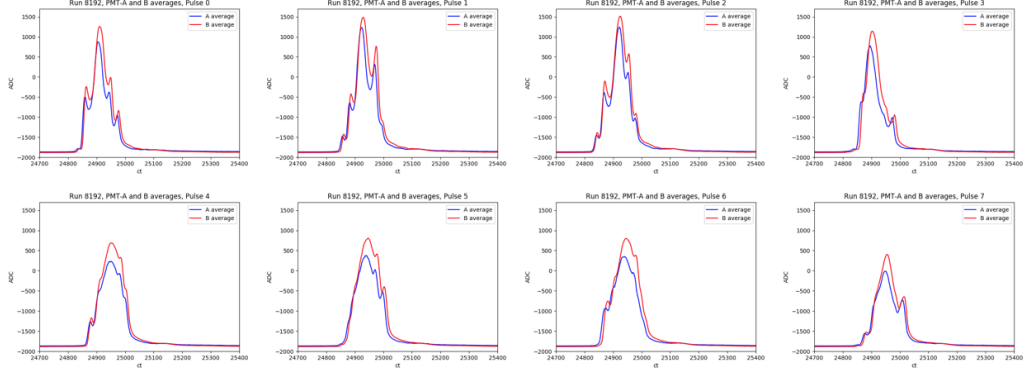


Figure 2.5: Shown are time profiles for the two PMTs (A and B) in the T0 counter for the 8 pulses we receive in an accelerator cycle/bunch/what. (careful here - not quite right) Each profile is an average of 100 such profiles. The x axis is in clock ticks (ct), each of which is 1.25 ns. (I will probably explain cts before this somewhere right?) PMT A is the low stats p.e. phototube and PMT B is the high stats p.e. phototube. Picture is too small, might want to rotate or replace it with something.

### 2.5.2 IBMS

There are two scintillating fiber detectors which monitor the beam as it passes through the inflector, the so-called inflector beam monitoring system (IBMS). See Figure 2.6. These devices are placed at the outside of the magnet yoke before injection into the back hole of the magnet, and at the entrance to the inflector. A third device is planned to be at or near the downstream end of the inflector (fix this later on). See Figure 2.7. These devices are used to verify the beam optics tune in the muon injection through the inflector and continuously diagnose beam properties as a handle on systematic problems. Probably cite something in this section - not the TDR since the IBMS was not included in the TDR.

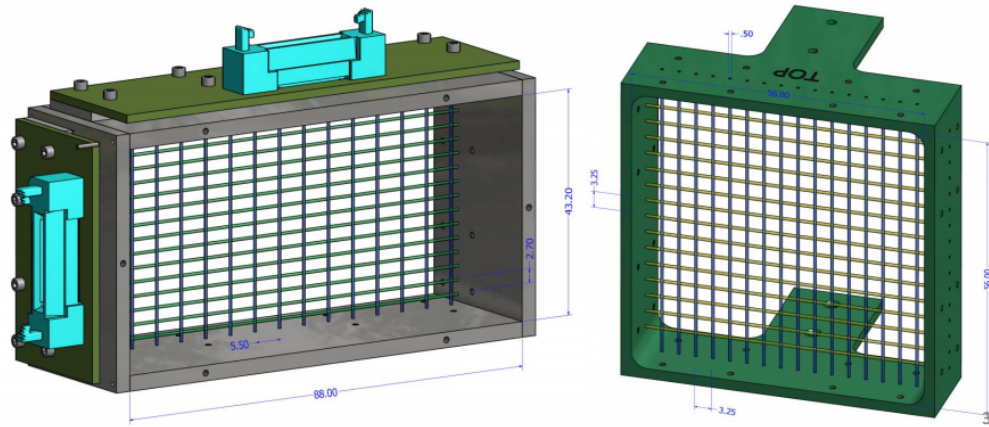


Figure 2·6: Simulation models of the IBMS 1 and 2 detectors. Scintillating fibers form an array which detect particles as they pass through them.



Figure 2·7: The positions of IBMS 1, 2, and the planned 3rd system are shown with respect to the vacuum chamber and inflector.

### 2.5.3 Fiber Harps

There are four scintillating fiber detectors located within the ring, two at the 180 degree position which measure the vertical and horizontal directions respectively, and similarly at the 270 degree position. One of these devices is shown in Figure 2·8. These ‘fiber harps’ serve to monitor beam properties at all times during a fill, including just after injection and during scraping. This is especially useful as a diagnostic tool as well as a measurement of the central beam position and CBO properties (have I talked about this yet?). Because the fiber harps are a destructive measurement of the beam, they are retractable and are only inserted in special runs in order to make said beam measurements. When they are inserted however they provide a wealth of useful information regarding the beam, as shown in Figure 2·9. Probably cite something in this section.

-DocDB 8366 -maybe find another docb/source

### 2.5.4 Calorimeters

Electromagnetic calorimeters measure the times and energies of decay positrons as they curl inward from the storage region. There are 24 calorimeters located symmetrically around the inside of the ring in close proximity to the vacuum chamber, as shown in Figure 2·10. They lie close to the storage region in order to measure a large fraction of the total number of observable decay positrons, including the high energy decay positrons which curl inward only slightly more than the muons themselves do. (max acceptance)

Each calorimeter consists of 54 channels of  $\text{PbF}_2$  crystals arrayed in a 6 high by 9 wide array, which measure Cerenkov light emitted by the incident positrons as they pass through the crystals [7]. (Picture of single calo and its crystals here.) Cerenkov light is naturally fast which improves timing resolution of the incoming hits. Each

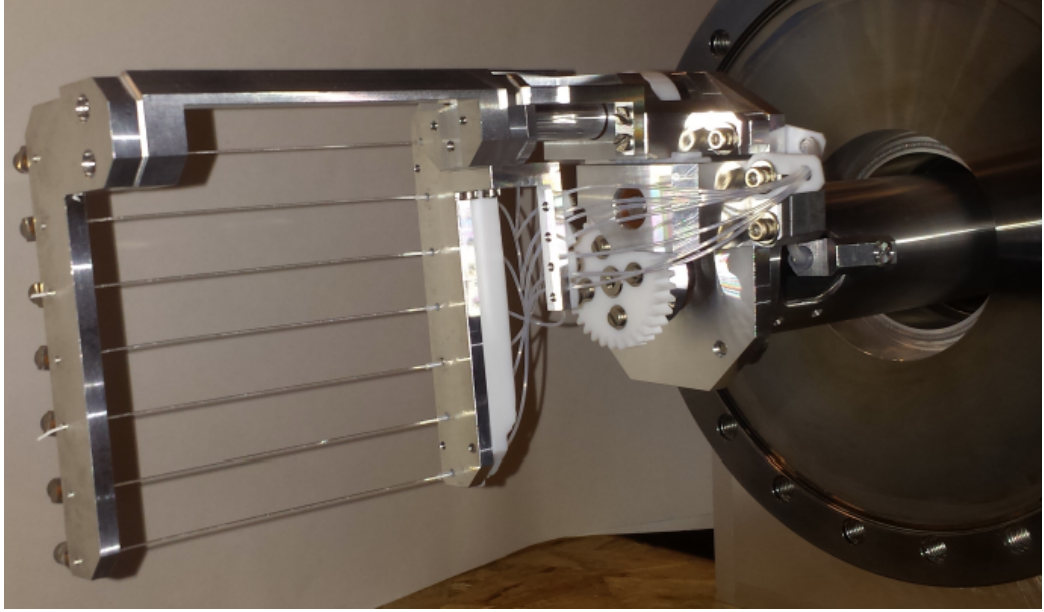


Figure 2.8: Picture of one of the fiber harps. A row of 7 scintillating fibers measures the beam intensity as a function of time at various vertical or horizontal components depending on which fiber harp is inserted.

crystal is  $2.5 \times 2.5 \times 14 \text{ cm}^3$  and is wrapped in black Tedlar® foil to reduce light transmission between crystals and improve position reconstruction, as well as reduce pulse width [8]. The light is read out by large area silicon photo-multiplier (SiPM) sensors. Each calorimeter sits on a board extending out from a cart containing the electronic which power the calorimeters and read out the data, as shown in Figure ?? This is to relocate magnetic material away from the field region to avoid perturbing the field and to remove sensitive electronics from the decay path region. Similarly, due to the close proximity to the storage region and by extension the magnetic field, the calorimeters, the encapsulating material, and the SiPMs are made from non-magnetic material.

In order to determine  $a_\mu$  to the precision goal, there are modest requirements on the performance of the calorimeters. They must have a relative energy resolution of better than 5% at 2 GeV, in order for proper event selection [6]. They must have

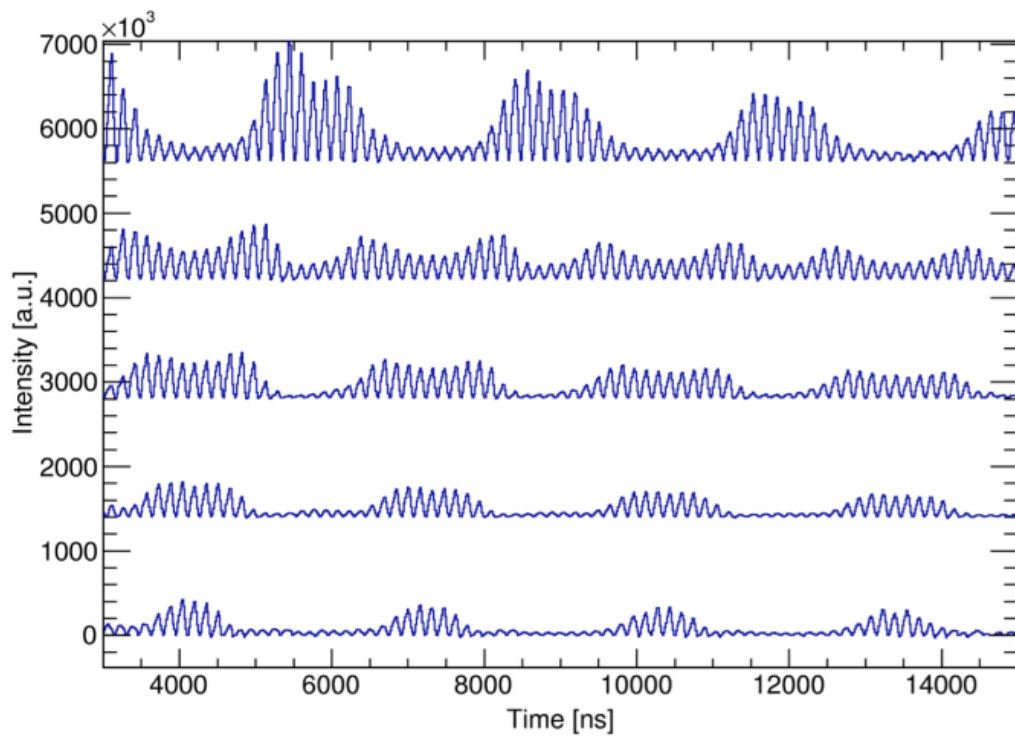


Figure 2.9: The fiber harps measure beam intensity as a function of time and fiber number. The middle spectrum is the output from the middle fiber, the upper spectra being fibers which are at successively greater radial positions, and the lower spectra being fibers which are at successively lower radial positions. The fast oscillations of the cyclotron frequency can be seen along with the slower oscillations of the CBO. This particular set of data was at a time or run when more beam was on the outside part of the storage region. (This last part is conjecture somewhat - maybe I should leave it out. I might honestly also want to leave out this whole picture, not sure..)

a timing resolution of better than 100 ps for positrons with greater than 100 MeV energy. The calorimeters must be able to resolve multiple incoming hits through temporal or spatial separation at 100% efficiency for time separations of greater than 5 ns in order to reduce the pileup systematic error due to the high rate. Finally, the gain of the measured hits must be stable to  $< 0.1\%$  over a 200  $\mu\text{s}$  time period within a fill, and unaffected by a pulse arriving in the same channel a few nanoseconds earlier. The long term gain stability over a time period of order seconds must be  $< 1\%$ . The SiPMs chosen satisfy these requirements (as well as the physical ones), due to their fast rise times and consistent pulse shapes. (Should this part be here? Or elsewhere? Before perhaps? Might need to update the gain numbers...)

(I've condensed quite a bit this section from the TDR - is that okay?)

A 12 bit waveform digitizer (WFD) samples each photodetector channel at a rate of 800 MSPS with a 1 Gb memory buffer and the data are transferred to a bank of GPU processors for on-line data processing [9]. The timing resolution of these WFDs is  $< 50$  ps for most pulse amplitudes.

Should I go into the calorimeter DAQ here? Or make that it's own section - how uniform are the DAQ systems for each detector system? Are the same sorts of modules and crates and WFDs used or what? If so it's own section might make sense, otherwise probably include small pieces at the end of each individual detector about the daq system

### 2.5.5 Laser Calibration System

In order to satisfy the gain requirements, a laser calibration system was put into place in order to monitor the SiPM responses over short times (fill level), and long term (days to years). By comparing a known signal to the SiPM output. At the front face of each calorimeter is a board containing prisms connected to fibers from the laser system which can be pulsed in-fill or out of fill for each crystal individually.

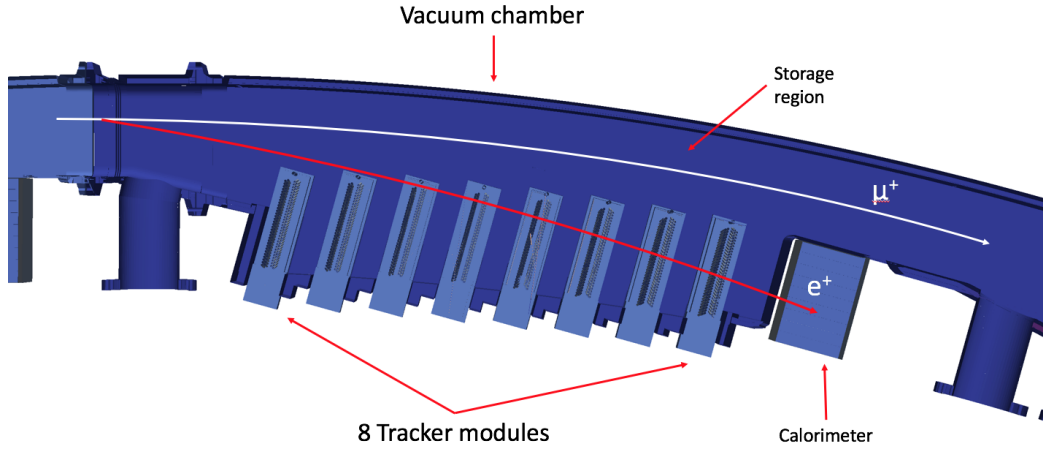


Figure 2.10: Birds eye view of a model of a vacuum chamber containing a tracker station, and the associated calorimeter. Muons pass around the ring in the center of the storage region which is contained within the bulk of the vacuum chamber. The muons decay to positrons, some of which then pass through the trackers or hit calorimeters. Each tracking station consists of 8 tracker modules.

-can pulse laser in fill, out of fill, and double pulse -mention the laser hut at all?  
probably not

[10] [11] [12]

### 2.5.6 Straw Trackers

The Muon  $g - 2$  Experiment at Fermilab uses straw tracking detectors to measure decay positron trajectories for the purpose of determining the muon beam distribution and its characteristics (and other things....). By fitting these tracks and extrapolating back to the average decay point, the beam can be characterized in a non-destructive fashion. See section blah. This is important because of the need for matching the average observed magnetic field of the decaying muons and their resulting decay positron directions which result in the  $\omega_a$  frequency.

The trackers are also useful for determining general beam diagnostics as well as the pitch correction and to a lesser extent the electric field correction (careful here).

Cross-checking separately for pileup removal, hit verification, etc. is a powerful tool. Combining them in order to provide the muon distribution that the calorimeters directly see for the  $\omega_a$  calculation is perhaps the most important role of the tracker. With three trackers, approximately 5% of decaying muons will result in measureable positron tracks assuming no pileup in the tracker, many of which do not hit the nearest calorimeter.

Each tracker module consists of 4 layers of 32 straws with a stereo angle of 7.5 degrees, the first two “U” layers oriented with the tops of the straws at a greater radial position, and the second two “V” layers oriented with the bottoms of the straws at a greater radial position. A tracking module is shown in Figure 2.11. There are 2 tracker stations located in front of calorimeters 13 and 19, or at approximately 180 and 270 degrees counting clockwise from the top most point of the ring where the inflector resides. Figure ?? shows this. (A third station sits empty after the inflector.) Each station consists of 8 tracking modules arranged in a staircase pattern that follows the curvature of the ring as seen in Figure 2.12.

In order to reduce the amount of multiple scattering within the straw tracking chambers as particles pass through them, the material of the straw trackers is minimized. Each straw is made of mylar foil, within which a  $25 \mu\text{m}$  radius tungsten wire resides, and is filled with Argon-Ethane gas [**something**]. Fast moving particles ionize the gas as they pass through it, and the resulting ions are drawn to the wire which is held at high voltage. When they reach the wire (and the mylar) a signal can be read out which tells us that a particle was seen to pass through the straw. By combining many such signals in a brief time span, we are able to construct tracks of incident particles. (See section blah.) The resolution of hits within the straws is approximately  $150 \mu\text{m}$  [**something**].

The signals of the straws are read out through...

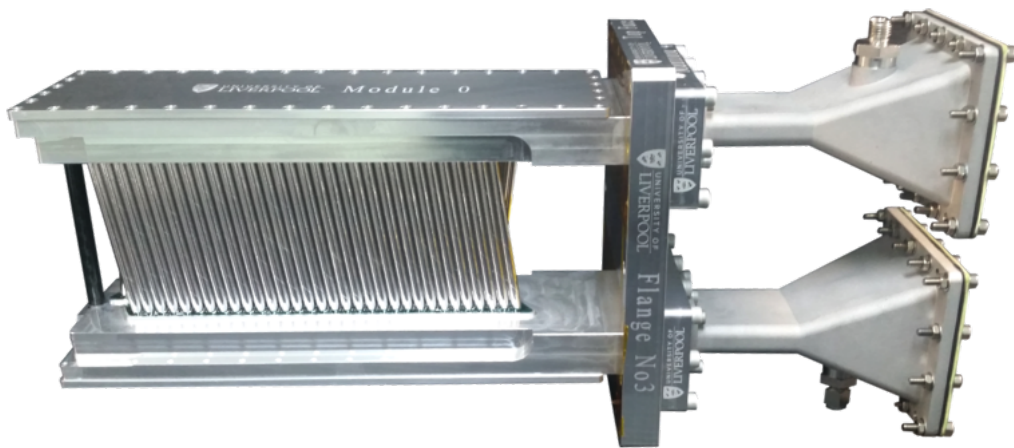


Figure 2.11: Shown is a picture of one of the many tracking modules used in the Muon  $g - 2$  experiment. The first layer of straws with a stereo angle of 7.5 degrees can be seen, with the other 3 straw layers hiding behind it. The beam direction is roughly into the page in this picture, to the left of the end of the module, and this view is what the decay positrons will see.

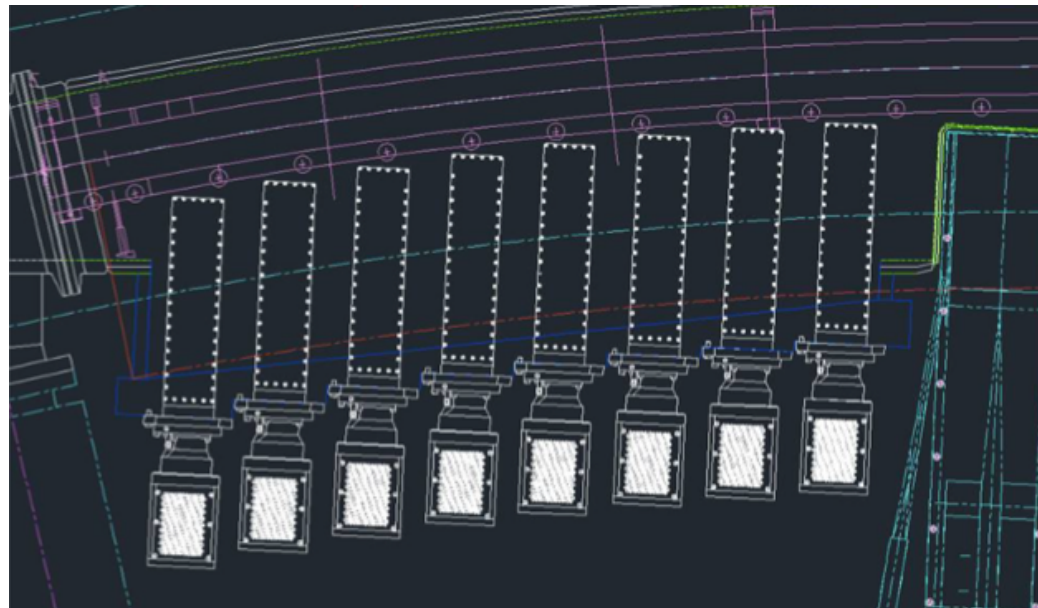


Figure 2.12: Tracker modules are arranged in the shown staircase pattern. In green and dark blue is the edge of the vacuum chamber (where the dark blue identifies the modification that was made to the old vacuum chambers), and it can be seen that vacuum chamber walls lie at the ends of the outside tracking modules. The position of a calorimeter can be seen in cyan at the right. The dark red spots are the locations of the outside magnet pole tips. From the shown geometry one can see that many positrons will hit either the tracker or the calorimeter but not both due to the acceptance differences.

## **Chapter 3**

# **Magnetic Field Measurement**

### **3.1 Trolley**

### **3.2 Opera Simulations**

Where does this section really go?

## Chapter 4

# Straw Tracking Analysis

### 4.1 Straw Tracking Intro

As was talked about briefly in section 2.5.6, the straw trackers are used to provide information about the muon beam, as well as info for the calorimeters. The straw track reconstruction is performed in several stages. The “Track Finding” stage takes incoming hits and decides which hits should be grouped together to form a single track for a single positron. The “Track Fitting” stage fits the measured positions of these individual hits and forms a single track describing the trajectory of the incident positron. Finally the “Track Extrapolation” stage takes the fitted track information and extrapolates the position and momentum components to the regions of interest, namely the storage region and the calorimeter.

-see the previous section for the hardware information... -Geane (Geometry and Error Propagation)

### 4.2 Track Finding

### 4.3 Track Fitting

The Geane fitting routines originated in Fortran with the EMC collaboration, and was used in the precursor E821 experiment as well as the PANDA experiment with some success [13], [14]. (I’m not actually aware of a useful reference for it’s use in E821, and there are some other instances of its use as well in other experiments. In E821

Run 1863, SubRun 25, Event 281, Island 66, Time 683689

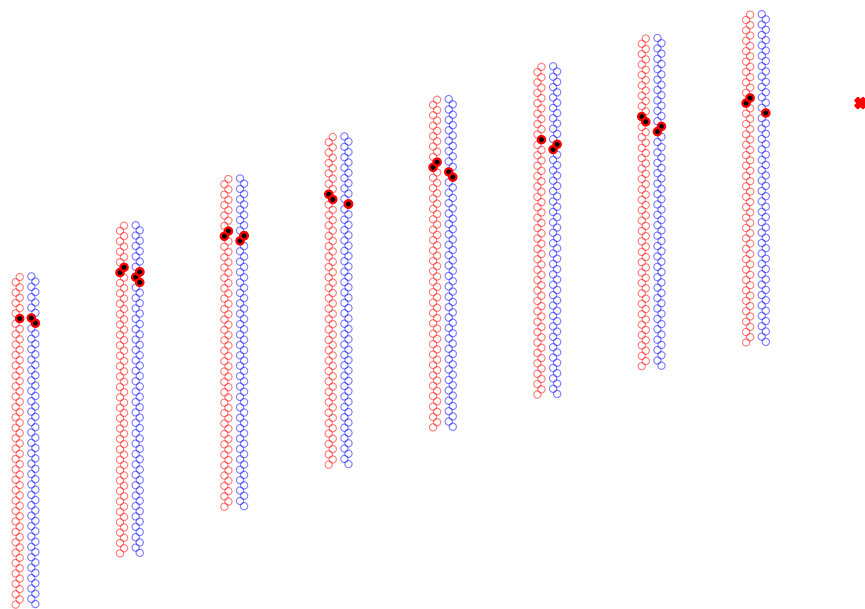


Figure 4·1: clean up and possibly replace

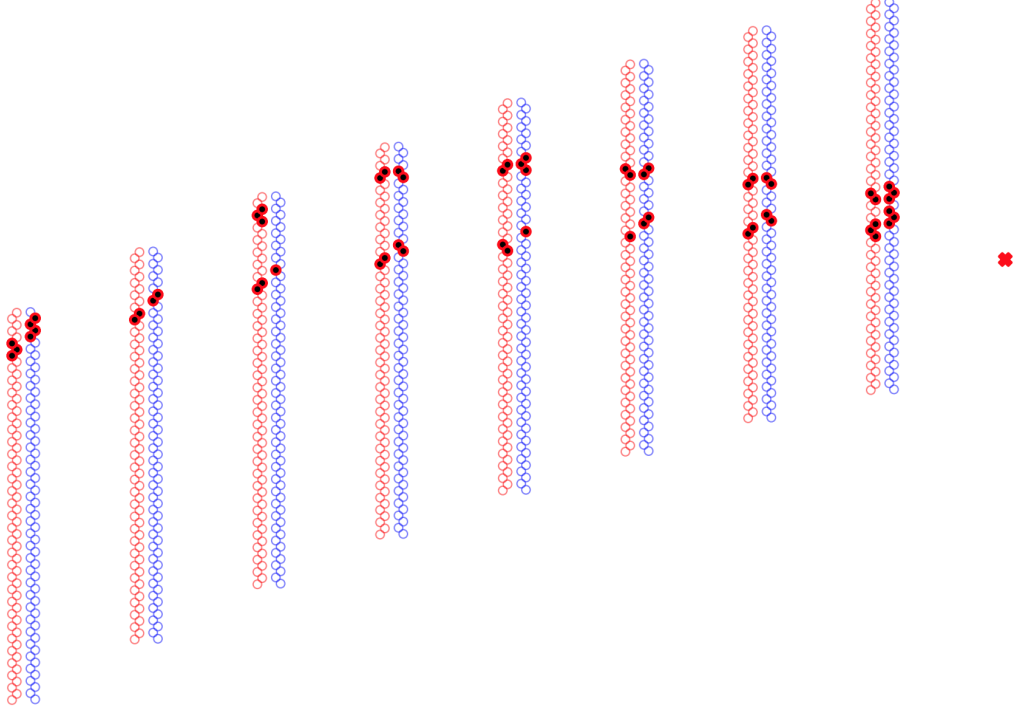


Figure 4·2: clean up and possibly replace

there was a single tracking chamber which was never put to full use.) The core error propagation routines were at some point added to Geant4 under the error\_propagation directory which is included in all default installs. The tracking code strengths lie with its direct implementation and access to the Geant4 geometry and field, and its ability to handle the field inhomogeneties. The Geane fitting algorithm code which makes use of the Geant4 error propagation routines follows the structure of [13] and is detailed in the Formalism section in this paper. It is a relatively straight forward least squares global  $\chi^2$  minimization algorithm.

Because of the proximity of the trackers to the muon beam, they will lie within a region of varying magnetic field. The radial field of the trackers rises from 0 Tesla at the outer ends to roughly .3 Tesla at the inner top and bottom ends, and the vertical field drops approximately 50% from the storage dipole field of 1.451 Tesla. Shown in Figures 4·3 and 4·4 is the location of the tracker with respect to the horizontal

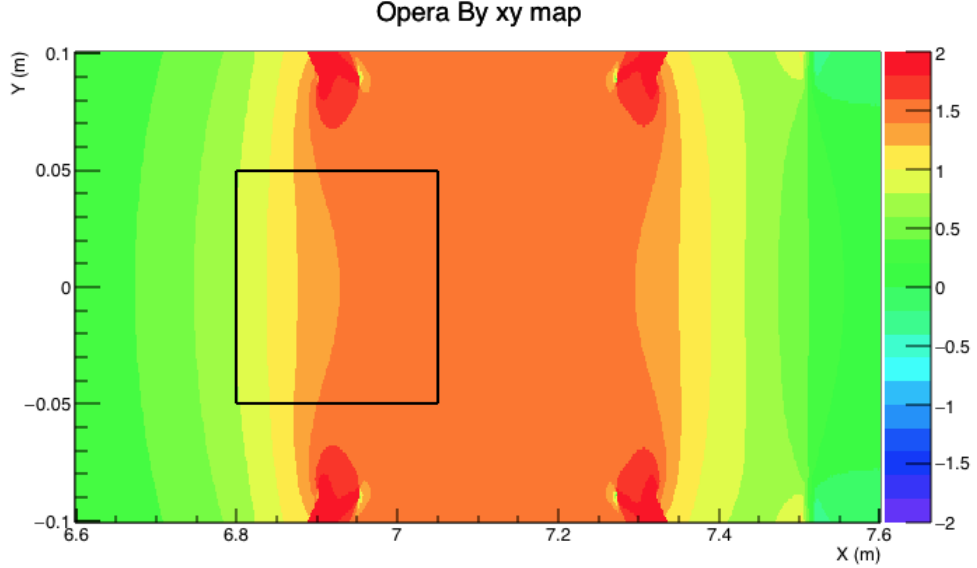


Figure 4.3: Shown is the vertical field of the  $g - 2$  magnet in and around the storage region as calculated in Opera 2D. The center of the storage region lies at 7.112 m along the x axis. The black box shows the rough location of the tracker with respect to the field (size exaggerated slightly). It can be seen that there is a large inhomogeneity within the tracker space, going from left to right.

and vertical fields respectively. These large field gradients over the tracking detector region and the long extrapolation distance back to the muon decay point are special to Muon  $g - 2$ . This is one of the main motivations for using the Geane fitting algorithm and routines, which has direct access to the field.

#### 4.3.1 Track Fitting Formalism

I recommend reading [13], Chapter 4 of [14], and [15] in order to best understand the fitting algorithm. However, due to the at times confusing notation, omitted equations or concepts, and differences between papers, I have attempted to summarize here the different sources and present the material in a more understandable and readable format. The implementation of the fitting algorithm into the code follows this section.

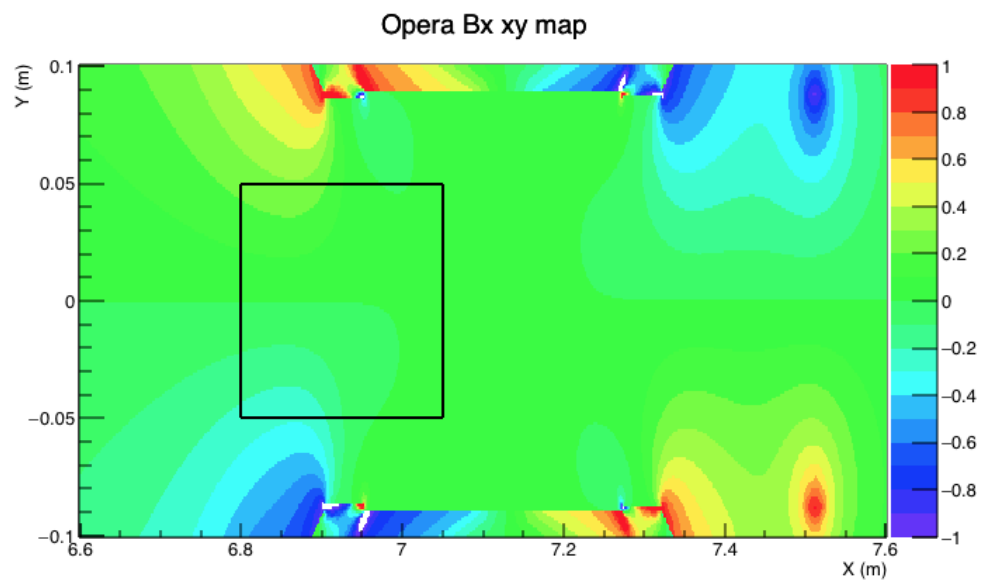


Figure 4.4: Shown is the radial field of the  $g - 2$  magnet in and around the storage region as calculated in Opera 2D. The center of the storage region lies at 7.112 m along the x axis. The black box shows the rough location of the tracker with respect to the field (size exaggerated slightly). It can be seen that there is a large homogeneity at the inner upper and lower ends compared to the right center. The shape of the pole pieces and tips can readily be seen.

One can define a  $\chi^2$  for a track in the usual way by dividing the residuals of measured and predicted track parameters by their errors:

$$\chi^2 = (\vec{p} - \vec{x})^T (\sigma^{-1}) (\vec{p} - \vec{x}), \quad (4.1)$$

where  $\vec{p}$  are predicted track parameters from a fit to the measured track parameters  $\vec{x}$ , and  $\sigma$  is a covariance matrix of errors on the fitted parameters. The Geant4 error propagation routines can be used to determine these predicted parameters and error matrices by propagating track parameters from some initial guesses. By minimizing this  $\chi^2$  with respect to the track parameters one can then fit and improve the track. The Geant4 error propagation routines propagate particles along their average trajectories neglecting the effects of discrete processes, using a helix equation along small enough steps where the change in the magnetic field is small. The predicted parameters are then a function of path length:

$$p_l = F_{l,l_0}(p_0), \quad (4.2)$$

where the path length can be defined how one wishes. In our system we have tracker planes defined at X positions, and limit path lengths to reach those planes. (From here on the dependence on path length or X position will be neglected, in favor of using plane indices.) In tandem, error matrices describing the expected distribution in true parameters about those predicted parameters due to said discrete process are also calculated:

$$\sigma^{ij} = \langle p^i p^j \rangle - \langle p^i \rangle \cdot \langle p^j \rangle, \quad (4.3)$$

where i and j are track parameter indices. These parameter vectors are 5x1 objects defined in some track representation, as described in the Coordinate Systems section. The propagation of these parameters and error matrices are done using transport

matrices, which express the infinitesimal changes in parameters at some plane (or path length) with respect to the parameters at some previous plane (or previous path length):

$$\delta p_N = T_{N,N-1} \delta p_{N-1}, \quad (4.4)$$

$$\sigma_N = T_{N,N-1} \sigma_{N-1} T_{N,N-1}^T. \quad (4.5)$$

Said transport and error matrices are 5x5 objects since the parameter vectors are 5x1 objects as described above. The calculation of these transport matrices, as well as details on the functional form of 4.2 are shown in [16].

With parameters defined on such planes, one can define the  $\chi^2$  as:

$$\chi^2 = \sum_{i=1}^N [(p_i(p) - x_i)^T (\sigma_i^{-1}) (p_i(p) - x_i)], \quad (4.6)$$

where  $p_i$  are the average predicted parameters from some general starting parameters  $p$ . At first order one can solely include the measurement errors on parameters, which fill in the diagonals of  $\sigma_i$ , if random processes can be neglected. Unmeasured parameters should have measurement errors of infinity (or some large value) along the diagonals in the code, which account for the fact that residuals for unmeasured parameters do not exist. When the error matrix is inverted all rows and columns of the matrix with these large numbers will fall to 0 in the  $\chi^2$ .

In order to get the best fit track, the  $\chi^2$  should be minimized with respect to the initial track parameters  $p$ , and evaluated at some chosen or fitted parameters:

$$\frac{\partial \chi^2}{\partial p} |_{p=p'_0} = 0, \quad (4.7)$$

resulting in

$$\begin{aligned} 0 = \sum_{i=1}^N & [(\frac{\partial p_i(p)}{\partial p}|_{p=p'_0})^T (\sigma_i^{-1})(p_i(p'_0) - x_i) \\ & + (p_i(p'_0) - x_i)^T \frac{\partial(\sigma_i^{-1})}{\partial p}|_{p=p'_0} (p_i(p'_0) - x_i) \\ & + (p_i(p'_0) - x_i)^T (\sigma_i^{-1}) (\frac{\partial p_i(p)}{\partial p}|_{p=p'_0})] \end{aligned} \quad (4.8)$$

where the 1st and 3rd terms are identical, and the 2nd term is small if one assumes that the error matrix doesn't change much with respect to the starting parameters. (Fair since most of the error comes from measurement, and as long as the initial guess is decent enough such that the path length through material doesn't change appreciably from one iteration to the next.) This simplifies to:

$$\sum_{i=1}^N T_{i0}^T (\sigma_i^{-1}) (p_i(p'_0) - x_i) = 0, \quad (4.9)$$

which is just the top term with

$$T_{i0} = \frac{\partial p_i(p)}{\partial p}. \quad (4.10)$$

To solve this make the substitution

$$p_i(p'_0) = p_i(p_0) + \frac{\partial p_i(p_0)}{\partial p} \Delta p_0 = p_i(p_0) + T_{i0} \Delta p_0, \quad (4.11)$$

where  $p'_0$  are the improved starting parameters for the next iteration calculated from the previous starting parameters  $p_0$ , and  $\Delta p_0$  are the changes in the starting parameters to improve the track. This equation can be plugged into the above if one makes the assumption that  $T_{i0}$  does not change much from one iteration to the next, which follows from the inherent nature of making small adjustments to the track in order to improve it.

After simplifying one arrives at

$$\Delta p_0 = \sigma_{p_0} \sum_{i=1}^N T_{i0}^T (\sigma_i^{-1}) (x_i - p_i(p_0)), \quad (4.12)$$

where

$$\sigma_{p_0} = \left[ \sum_{i=1}^N T_{i0}^T (\sigma_i^{-1}) T_{i0} \right]^{-1}, \quad (4.13)$$

is the 5x5 covariance matrix of fitted parameters on the starting plane, whose diagonals describe the errors in the 5 track parameters on that plane and in the region close to it. (The fit does not directly return fit errors for track parameters on other planes.)  $\Delta p_0$  along with  $\chi^2$  is exactly what we want to determine since that is what allows us to fit and improve the track from iteration to iteration.

However, since random processes should not be neglected for optimal tracking results, it makes more sense to return to the original  $\chi^2$  in equation 4.1, only now the included matrix and vector objects are combined into one large linear algebra equation. Instead of a sum over N 5x1 objects multiplying 5x5 error matrices, the vectors are combined into a single 5Nx1 vector multiplying a single 5Nx5N matrix. The 5x5 diagonal blocks of this large error matrix should now include the effects due to material processes as calculated in Geant from equation 4.3 as well as the measurement errors.

Because now parameters at one plane are no longer independent of the parameters at other planes, due to correlations from these random processes, it's necessary to add off-diagonal elements into the large error matrix. These 5x5 blocks come from

$$\sigma_{MN} = T_{MN} \sigma_N, \quad (4.14)$$

for the top diagonals, and the transpose for the bottom diagonals, where M and N are two separate planes within the detector. ( $\sigma_N$  is the error matrix on plane N

calculated from the starting plane.) This follows from equation 4.3 evaluated at plane M with respect to a path length from plane N, and not plane 0, which is equivalent to 4.14.

You can then minimize the  $\chi^2$  in the same way, only again with the matrix objects being aggregates of the per plane objects:

$$\Delta \vec{p}_0 = \sigma_{p_0} \tau^T \sigma^{-1} (\vec{x} - \vec{p}), \quad (4.15)$$

$$\sigma_{p_0} = [\tau^T \sigma^{-1} \tau]^{-1}, \quad (4.16)$$

where  $\tau$  is the combined transport matrices from the individual 5x5 matrices, a 5Nx5 object.

The unmeasured parameter errors of infinity still come into play in the final calculation in the same was as before. Because however these matrix objects are very large, and the tracking must have a certain amount of speed in order to keep up with data, it is useful to reduce the size of these matrices. (It also makes things easier programming wise. Note that there are other some other ways to speed things up, specifically the banded inversion method as described in reference [15]. This method was not used in favor of getting the code working in the simpler form in the first place, but it is a possibility in the future to use this technique to speed things up even more.) It suffices to simply remove all rows and columns where said infinity values exist in the error matrix. This is mathematically equivalent to inverting the error matrix with the infinities included, which make all rows and columns where they exist go to zero. The associated unmeasured parameter rows in the residual vector and transport matrices must similarly be removed. This results in an Nx1 residual vector, NxN error matrix, 5xN combined transport matrix transpose, which multiply against the 5x5 covariance matrix out front to still result in a 5x1 fix to the starting

parameters, and a scalar  $\chi^2$  value. (Note that these element removals should be done just before the final calculation, and not higher up in the algebra, otherwise plane correlations are not properly calculated.)

By calculating the last two equations one can fit the track, acquire a  $\chi^2$  describing the degree of the fit, determine how the track parameters can be improved at the starting point, and calculate errors on those starting parameters. This algorithm can be iterated a number of times to get a best fit track until successive iterations produce no improvement, where usually 3 or 4 iterations is enough. Note that there is remarkable robustness with respect to the initial starting parameters in fitting the track. Of course if the initial starting parameters are too poor, then the fit will not converge. All of these calculations are completed within the GeaneFitter.cc file within the framework.

#### 4.4 Track Extrapolation

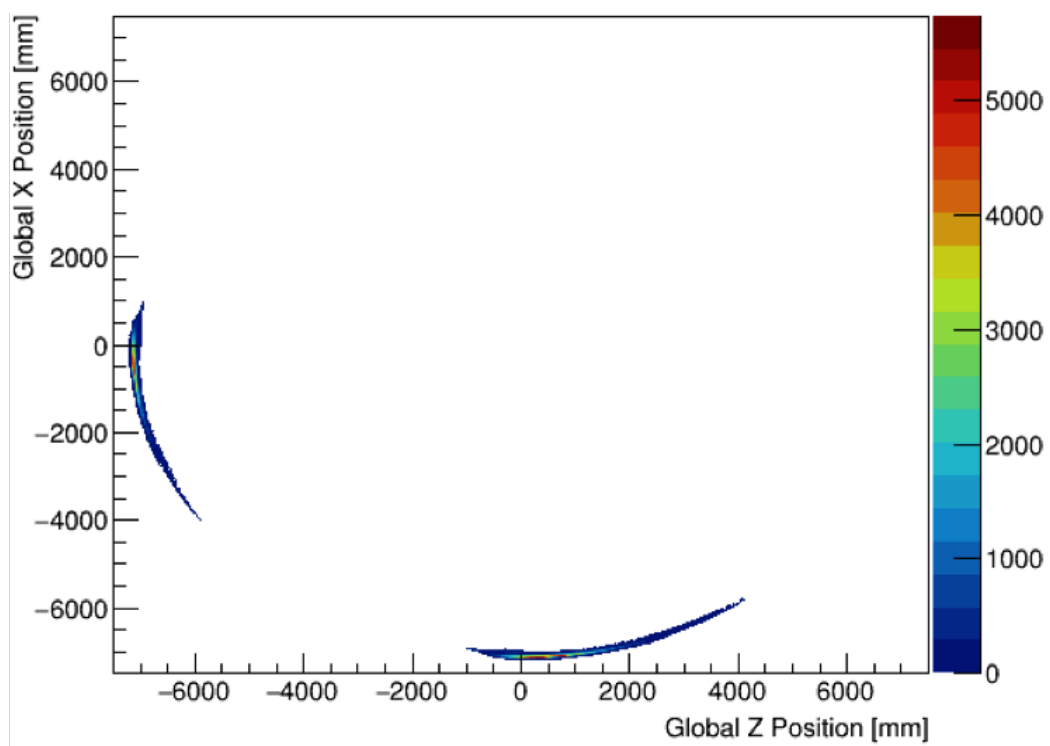


Figure 4·5: preliminary replace at some point

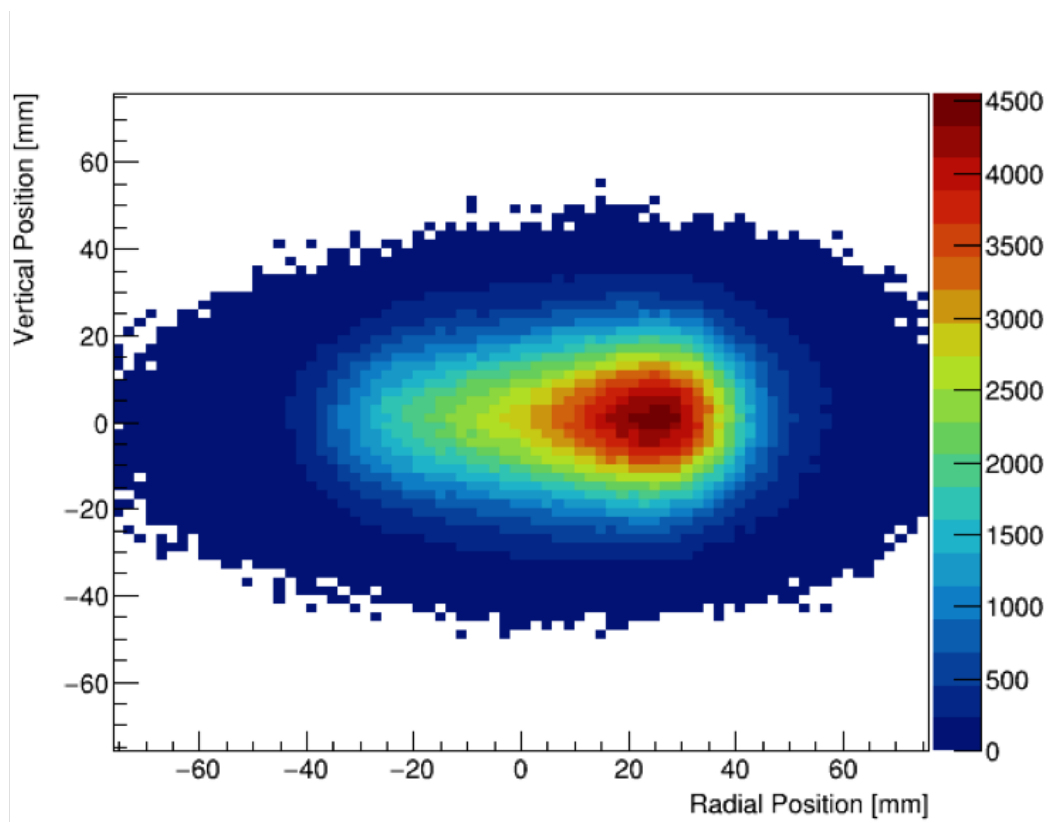


Figure 4·6: preliminary replace at some point

## Chapter 5

# $\omega_a$ Measurement

### 5.1 Data

### 5.2 Spectra Making

#### 5.2.1 Clustering

#### 5.2.2 Histogramming

### 5.3 Fitting

### 5.4 Systematic Errors

# Chapter 6

## Conclusion

### 6.1 Final Value

test4

## Appendix A

# $g$ for Spin-1/2 Particles and Beyond

This was taken from my old HEP2 class report paper - go back and clean this up/improve it.

The derivation contained here is taken and simplified from Reference [17]. Starting with the Dirac equation

$$(i\gamma^\mu \partial_\mu - m - e\gamma^\mu A_\mu)\psi = 0 \quad (\text{A.1})$$

and multiplying by

$$(i\gamma^\mu \partial_\mu + m - e\gamma^\mu A_\mu)\psi = 0, \quad (\text{A.2})$$

where the sign on  $m$  is reversed, you arrive at the equation

$$[(i\partial_\mu - eA_\mu)(i\partial_\nu - eA_\nu)\gamma^\mu\gamma^\nu - m^2]\psi = 0. \quad (\text{A.3})$$

This can be split this into its symmetric and antisymmetric parts:

$$\begin{aligned} & \left(\frac{1}{4}\{i\partial_\mu - eA_\mu, i\partial_\nu - eA_\nu\}\{\gamma^\mu, \gamma^\nu\}\right. \\ & \left. + \frac{1}{4}[i\partial_\mu - eA_\mu, i\partial_\nu - eA_\nu][\gamma^\mu, \gamma^\nu] - m^2\right)\psi = 0 \end{aligned} \quad (\text{A.4})$$

Using the identities

$$\frac{i}{2}[\gamma^\mu, \gamma^\nu] = \sigma^{\mu\nu} \quad (\text{A.5})$$

and

$$\begin{aligned} & [i\partial_\mu - eA_\mu, i\partial_\nu - eA_\nu] \\ &= -ie[\partial_\mu A_\nu - \partial_\nu A_\mu] = -ieF_{\mu\nu} \end{aligned} \quad (\text{A.6})$$

where  $\sigma^{\mu\nu}$  is related to the spin of the particle and  $F_{\mu\nu}$  is the electromagnetic field tensor, one arrives at the form

$$((i\partial_\mu - eA_\mu)^2 - \frac{e}{2}F_{\mu\nu}\sigma^{\mu\nu} - m^2)\psi = 0. \quad (\text{A.7})$$

Expanding out the tensor objects

$$\frac{e}{2}F_{\mu\nu}\sigma^{\mu\nu} = -e \begin{pmatrix} (\vec{B} + i\vec{E}) \cdot \vec{\sigma} \\ (\vec{B} - i\vec{E}) \cdot \vec{\sigma} \end{pmatrix} \quad (\text{A.8})$$

and forming a new covariant derivative

$$\not{D}^2 = D_\mu^2 + \frac{e}{2}F_{\mu\nu}\sigma^{\mu\nu} \quad (\text{A.9})$$

where  $D_\mu^2$  is your ordinary covariant derivative, by moving to momentum space you can arrive at the equation

$$\frac{(H + eA)^2}{2m}\psi = \left(\frac{m}{2} + \frac{(\vec{p} + e\vec{A})^2}{2m}\right) - 2\frac{e}{2m}\vec{B} \cdot \vec{s} \pm i\frac{e}{m}\vec{E} \cdot \vec{s}\psi. \quad (\text{A.10})$$

Lo and behold, you have arrived at the Dirac  $g = 2$  result, contained in front of the magnetic piece in the form of Equation ??.

How then does such a term change at loop level? Most generally the vertex of a particle interacting with a magnetic field through the mediation of a photon can be represented by

$$iM^\mu = \bar{u}(q_2)(f_1\gamma^\mu + f_2p^\mu + f_3q_1^\mu + f_4q_2^\mu)u(q_1) \quad (\text{A.11})$$

where  $q_1$  and  $q_2$  are the ingoing and outgoing four-momenta respectively, which can be constrained on-shell, and  $p$  is the four-momenta of the photon, which is off-shell. The  $f_i$  are in general contractions of four-momenta and gamma matrices. By using the Gordon identity

$$\begin{aligned} & \bar{u}(q_2)(q_1^\mu + q_2^\mu)u(q_1) \\ &= (2m)\bar{u}(q_2)\gamma^\mu u(q_1) + i\bar{u}(q_2)\sigma^{\mu\nu}(q_1^\nu - q_2^\nu)u(q_1) \end{aligned} \quad (\text{A.12})$$

any Feynman diagram can be reorganized into the form

$$iM^\mu = (-ie)\bar{u}[F_1(\frac{p^2}{m^2})\gamma^\mu + \frac{i\sigma^{\mu\nu}}{2m}p_\nu F_2(\frac{p^2}{m^2})]u, \quad (\text{A.13})$$

where  $F_1$  and  $F_2$  are form factors. One notices that the  $F_2$  piece is reminiscent of our magnetic dipole moment form that we derived from the Dirac equation. So the problem now becomes for any Feynman diagram calculation in any theory, at any order, to solve for this  $F_2$  to determine the contribution to the magnetic dipole moment.

## Appendix B

# Ratio Method Derivation

### B.1 Ratio Function

Consider the 5 parameter function:

$$N_5(t) = N_0 e^{-t/\tau} (1 + A \cos(\omega_a t + \phi)), \quad (\text{B.1})$$

which describes some ideal dataset in histogram format. Here  $\phi$  will be set to zero for simplicity. Now define the variables  $u_+(t)$ ,  $u_-(t)$ ,  $v_1(t)$ , and  $v_2(t)$  as

$$\begin{aligned} u_+(t) &= \frac{1}{4} N_5(t + T/2) \\ u_-(t) &= \frac{1}{4} N_5(t - T/2) \\ v_1(t) &= \frac{1}{4} N_5(t) \\ v_2(t) &= \frac{1}{4} N_5(t), \end{aligned} \quad (\text{B.2})$$

where the  $1/4$  out front reflects randomly splitting the whole dataset into 4 equally weighted sub-datasets, and  $T$  is the g-2 period known to high precision,  $\mathcal{O}(10^{-6})$ . This corresponds to a weighting of 1:1:1:1 between the datasets. To be explicit here regarding the signs, the counts that are filled into the histogram described by  $u_+$  have their times shifted as  $t \rightarrow t - T/2$ , which is what the function  $N_5(t + T/2)$  describes,

and vice versa for  $u_-$ . To form the ratio define the variables:

$$\begin{aligned} U(t) &= u_+(t) + u_-(t) \\ V(t) &= v_1(t) + v_2(t) \\ R(t) &= \frac{V(t) - U(t)}{V(t) + U(t)}. \end{aligned} \tag{B.3}$$

Plugging in and dividing the common terms ( $N_0 e^{-t/\tau}/4$ ),

$$R(t) = \frac{2(1 + A \cos(\omega_a t)) - e^{-T/2\tau}(1 + A \cos(\omega_a t + \omega_a T/2)) - e^{T/2\tau}(1 + A \cos(\omega_a t - \omega_a T/2))}{2(1 + A \cos(\omega_a t)) + e^{-T/2\tau}(1 + A \cos(\omega_a t + \omega_a T/2)) + e^{T/2\tau}(1 + A \cos(\omega_a t + \omega_a T/2))}. \tag{B.4}$$

Now set  $\omega_a T/2 = \delta$ , and note that  $T$  is really

$$\begin{aligned} T &= T_{guess} = \frac{2\pi}{\omega_a} + \Delta T, \\ \Delta T &= T_{guess} - T_{true}. \end{aligned} \tag{B.5}$$

Being explicit,

$$\delta = \frac{\omega_a}{2} T_{guess} = \frac{\omega_a}{2} \left( \frac{2\pi}{\omega_a} + \Delta T \right) = \pi + \pi \frac{\Delta T}{T_{true}} = \pi + \pi(\delta T), \tag{B.6}$$

and  $\delta$  can be redefined as

$$\delta = \pi(\delta T), \tag{B.7}$$

by flipping the sign of any cosine terms that contain  $\delta$ .

Then, using the trig identity

$$\cos(a \pm b) = \cos(a) \cos(b) \mp \sin(a) \sin(b) \tag{B.8}$$

so that

$$\begin{aligned}\cos(\omega_a t \pm \delta) &= \cos(\omega_a t) \cos \delta \mp \sin(\omega_a t) \sin \delta \\ &\approx \cos(\omega_a t)(1 - \delta^2) \mp \sin(\omega_a t)\delta \\ &\approx \cos(\omega_a t),\end{aligned}\tag{B.9}$$

since  $\delta \sim O(10^{-5})$ , the ratio becomes

$$R(t) \approx \frac{2(1 + A \cos(\omega_a t)) - (1 - A \cos(\omega_a t))(e^{-T/2\tau} + e^{T/2\tau})}{2(1 + A \cos(\omega_a t)) + (1 - A \cos(\omega_a t))(e^{-T/2\tau} + e^{T/2\tau})}.\tag{B.10}$$

Expanding

$$e^{\pm T/2\tau} = 1 \pm \frac{T}{2\tau} + \frac{1}{2} \left( \frac{T}{2\tau} \right)^2 \pm \dots,\tag{B.11}$$

replacing and simplifying,

$$R(t) \approx \frac{A \cos(\omega_a t) - C(1 - A \cos(\omega_a t))}{1 + C(1 - A \cos(\omega_a t))},\tag{B.12}$$

where

$$C = \frac{1}{16} \left( \frac{T}{\tau} \right)^2 \approx 2.87 * 10^{-4}.\tag{B.13}$$

Using the expansion

$$f(x) = \frac{1}{1+x} = 1 - x + x^2 - \dots, \quad |x| < 1,\tag{B.14}$$

and since  $C$  is small, the denominator can be manipulated such that

$$\begin{aligned}R(t) &\approx (A \cos(\omega_a t)) - C(1 - A \cos(\omega_a t))(1 - C(1 - A \cos(\omega_a t))) \\ &\approx A \cos(\omega_a t) - C + CA^2 \cos^2(\omega_a t),\end{aligned}\tag{B.15}$$

after dropping terms of  $\mathcal{O}(C^2)$  and higher. In practice the last term is omitted since

it has a minimal effect on the fitted value of  $\omega_a$  [cite], and one arrives at

$$R(t) \approx A \cos(\omega_a t) - C, \quad (\text{B.16})$$

the conventional 3 parameter ratio function.

In order to avoid approximations one can instead weight the counts in the histograms as

$$u_+(t) : u_-(t) : v_1(t) : v_2(t) = e^{T/2\tau} : e^{-T/2\tau} : 1 : 1, \quad (\text{B.17})$$

so that

$$\begin{aligned} u_+(t) &= \frac{e^{T/2\tau}}{2 + e^{T/2\tau} + e^{-T/2\tau}} N_5(t + T/2) \\ u_-(t) &= \frac{e^{-T/2\tau}}{2 + e^{T/2\tau} + e^{-T/2\tau}} N_5(t - T/2) \\ v_1(t) &= \frac{1}{2 + e^{T/2\tau} + e^{-T/2\tau}} N_5(t) \\ v_2(t) &= \frac{1}{2 + e^{T/2\tau} + e^{-T/2\tau}} N_5(t). \end{aligned} \quad (\text{B.18})$$

(These factors out front aren't so far off from 1/4 since  $e^{\pm T/2\tau} \approx e^{\pm 4.35/2*64.4} \approx 1.034, .967$ .) Then instead  $R(t)$  becomes

$$R(t) = \frac{2(1 + A \cos(\omega_a t)) - (1 - A \cos(\omega_a t + \delta)) - (1 - A \cos(\omega_a t - \delta))}{2(1 + A \cos(\omega_a t)) + (1 - A \cos(\omega_a t + \delta)) + (1 - A \cos(\omega_a t - \delta))}, \quad (\text{B.19})$$

where the  $e^{\pm T/2\tau}$  terms out front now cancel. Using Equation B.9 again and this time avoiding approximations in  $\delta$ ,

$$R(t) = \frac{2A \cos(\omega_a t)(1 + \cos \delta)}{4 + 2A \cos(\omega_a t)(1 - \cos \delta)}, \quad (\text{B.20})$$

after simplifying. In the limit that

$$\delta = \pi(\delta T) \rightarrow 0 \quad (\text{B.21})$$

since  $\delta T$  is small,

$$R(t) \approx A \cos(\omega_a t), \quad (\text{B.22})$$

with the only approximation being made at  $\mathcal{O}(\delta^2) \sim \mathcal{O}(10^{-10})$ .

Finally, while the 3 parameter ratio function suffices for fits to data containing slow modulations, it does not suffice for faster oscillation features. In that case it is more useful to fit with the non-approximated or simplified version of the ratio,

$$\begin{aligned} R(t) &= \frac{v_1(t) + v_2(t) - u_+(t) - u_-(t)}{v_1(t) + v_2(t) + u_+(t) + u_-(t)}, \\ &= \frac{2f(t) - f_+(t) - f_-(t)}{2f(t) + f_+(t) + f_-(t)}, \end{aligned} \quad (\text{B.23})$$

where

$$\begin{aligned} f(t) &= C(t)(1 + A \cos(\omega_a t + \phi)) \\ f_{\pm}(t) &= f(t \pm T_a/2), \end{aligned} \quad (\text{B.24})$$

and  $C(t)$  can encode any other effects in the data that need to be fitted for, such as the CBO,

$$C(t) = 1 + A_{cbo} \cdot e^{-t/\tau_{cbo}} \cdot \cos(\omega_{cbo}t + \phi_{cbo}). \quad (\text{B.25})$$

Additionally, any other fit parameters such as  $A$  or  $\phi$  can be made a function of  $t$ . Using the non-approximated form for the final fit function gives greater confidence in the fit results for the high precision  $\omega_a$  extraction necessary for the experimental measurement.

## B.2 Ratio Function Errors

In order to determine the errors on our fit function, Equation B.3, we use standard error propagation:

$$\sigma_R(t)^2 = \left(\frac{\partial R(t)}{\partial V(t)}\right)^2 \delta V(t)^2 + \left(\frac{\partial R(t)}{\partial U(t)}\right)^2 \delta U(t)^2 \quad (\text{B.26})$$

This works because  $V(t)$  and  $U(t)$  are statistically independent datasets. Using standard error propagation again,

$$\begin{aligned} \delta V(t)^2 &= \delta v_1(t)^2 + \delta v_2(t)^2 = v_1(t) + v_2(t) = V(t), \\ \delta U(t)^2 &= \delta u_+(t)^2 + \delta u_-(t)^2 = u_+(t) + u_-(t) = U(t). \end{aligned} \quad (\text{B.27})$$

Calculating out and simplifying the partial derivatives, (and this time dropping the  $t$ 's),

$$\begin{aligned} \frac{\partial R}{\partial V} &= \frac{2U}{(V+U)^2}, \\ \frac{\partial R}{\partial U} &= \frac{-2V}{(V+U)^2}. \end{aligned} \quad (\text{B.28})$$

Combining and simplifying, we arrive at the error formula:

$$\sigma_R^2 = \frac{4UV}{(V+U)^3} = \frac{1-R^2}{(V+U)} \quad (\text{B.29})$$

See Appendix B.4 in John Paley's thesis [18] for a calculation of the ratio method errors. They are derived using standard error propagation.

# Bibliography

- [1] G. W. Bennett et al. “Final Report of the Muon E821 Anomalous Magnetic Moment Measurement at BNL”. In: *Phys. Rev.* D73 (2006), p. 072003. DOI: [10.1103/PhysRevD.73.072003](https://doi.org/10.1103/PhysRevD.73.072003). arXiv: [hep-ex/0602035 \[hep-ex\]](https://arxiv.org/abs/hep-ex/0602035).
- [2] Alexander Keshavarzi, Daisuke Nomura, and Thomas Teubner. “Muon  $g-2$  and  $\alpha(M_Z^2)$ : a new data-based analysis”. In: *Phys. Rev.* D97.11 (2018), p. 114025. DOI: [10.1103/PhysRevD.97.114025](https://doi.org/10.1103/PhysRevD.97.114025). arXiv: [1802.02995 \[hep-ph\]](https://arxiv.org/abs/1802.02995).
- [3] Joshua Ellis. “TikZ-Feynman: Feynman diagrams with TikZ”. In: *Comput. Phys. Commun.* 210 (2017), pp. 103–123. DOI: [10.1016/j.cpc.2016.08.019](https://doi.org/10.1016/j.cpc.2016.08.019). arXiv: [1601.05437 \[hep-ph\]](https://arxiv.org/abs/1601.05437).
- [4] Max Dohse. “TikZ-FeynHand: Basic User Guide”. In: (2018). arXiv: [1802.00689 \[cs.OH\]](https://arxiv.org/abs/1802.00689).
- [5] Diktys Stratakis et al. “Accelerator performance analysis of the Fermilab Muon Campus”. In: *Phys. Rev. Accel. Beams* 20.11 (2017), p. 111003. DOI: [10.1103/PhysRevAccelBeams.20.111003](https://doi.org/10.1103/PhysRevAccelBeams.20.111003). arXiv: [1803.00597 \[physics.acc-ph\]](https://arxiv.org/abs/1803.00597).
- [6] J. Grange et al. “Muon ( $g-2$ ) Technical Design Report”. In: (2015). arXiv: [1501.06858 \[physics.ins-det\]](https://arxiv.org/abs/1501.06858).
- [7] A. T. Fienberg et al. “Studies of an array of  $\text{PbF}_2$  Cherenkov crystals with large-area SiPM readout”. In: *Nucl. Instrum. Meth.* A783 (2015), pp. 12–21. DOI: [10.1016/j.nima.2015.02.028](https://doi.org/10.1016/j.nima.2015.02.028). arXiv: [1412.5525 \[physics.ins-det\]](https://arxiv.org/abs/1412.5525).
- [8] J. Kaspar et al. “Design and performance of SiPM-based readout of  $\text{PbF}_2$  crystals for high-rate, precision timing applications”. In: *JINST* 12.01 (2017), P01009. DOI: [10.1088/1748-0221/12/01/P01009](https://doi.org/10.1088/1748-0221/12/01/P01009). arXiv: [1611.03180 \[physics.ins-det\]](https://arxiv.org/abs/1611.03180).
- [9] David A. Sweigart. “A new MicroTCA-based waveform digitizer for the Muon  $g-2$  experiment”. In: *PoS ICHEP2016* (2016), p. 845. DOI: [10.22323/1.282.0845](https://doi.org/10.22323/1.282.0845). arXiv: [1612.05145 \[physics.ins-det\]](https://arxiv.org/abs/1612.05145).
- [10] A. Anastasi et al. “Test of candidate light distributors for the muon ( $g-2$ ) laser calibration system”. In: *Nucl. Instrum. Meth.* A788 (2015), pp. 43–48. DOI: [10.1016/j.nima.2015.03.071](https://doi.org/10.1016/j.nima.2015.03.071). arXiv: [1504.00132 \[physics.ins-det\]](https://arxiv.org/abs/1504.00132).
- [11] A. Anastasi et al. “Electron beam test of key elements of the laser-based calibration system for the muon  $g-2$  experiment”. In: *Nucl. Instrum. Meth.* A842 (2017), pp. 86–91. DOI: [10.1016/j.nima.2016.10.047](https://doi.org/10.1016/j.nima.2016.10.047). arXiv: [1610.03210 \[physics.ins-det\]](https://arxiv.org/abs/1610.03210).

- [12] A. Anastasi et al. “The laser control of the muon  $g - 2$  experiment at Fermilab”. In: *JINST* 13.02 (2018), T02009. DOI: [10.1088/1748-0221/13/02/T02009](https://doi.org/10.1088/1748-0221/13/02/T02009).
- [13] V. Innocente, M. Maire, and E. Nagy. “GEANE: Average tracking and error propagation package”. In: *MC 91: Detector and event simulation in high-energy physics. Proceedings, Workshop, Amsterdam, Netherlands, April 8-12, 1991.* 1991, pp. 58–78. URL: [http://innocentonnice.web.cern.ch/innocentonnice/napoli99/geane\\_manual.ps](http://innocentonnice.web.cern.ch/innocentonnice/napoli99/geane_manual.ps).
- [14] Lia Lavezzi. “The fit of nuclear tracks in high precision spectroscopy experiments”. pp. 57-86. PhD thesis. Pavia U., 2007. URL: [http://bamboo.pv.infn.it/doc/L\\_Lavezzi.pdf](http://bamboo.pv.infn.it/doc/L_Lavezzi.pdf).
- [15] V. Innocente and E. Nagy. “Trajectory fit in presence of dense materials”. In: *Nucl. Instrum. Meth.* A324 (1993), pp. 297–306. DOI: [10.1016/0168-9002\(93\)90992-Q](https://doi.org/10.1016/0168-9002(93)90992-Q).
- [16] A. Strandlie and W. Wittek. “Derivation of Jacobians for the propagation of covariance matrices of track parameters in homogeneous magnetic fields”. In: *Nucl. Instrum. Meth.* A566 (2006), pp. 687–698.
- [17] M. Schwartz. *Quantum Field Theory and the Standard Model*. Cambridge University Press, 2014.
- [18] J. Paley. “Measurement of the Anomalous Magnetic Moment of the Negative Muon to 0.7 Parts Per Million”. PhD thesis. Boston University, 2004.

# **CURRICULUM VITAE**

## **Joe Graduate**

Basically, this needs to be worked out by each individual, however the same format, margins, typeface, and type size must be used as in the rest of the dissertation.